This document is downloaded from DR-NTU (https://dr.ntu.edu.sg)
Nanyang Technological University, Singapore.

Direct band gap mixed-valence organic-inorganic gold perovskite as visible light absorbers

Ghosh, Biplab; Febriansyah, Benny; Harikesh, Padinhare Cholakkal; Koh, Teck Ming; Hadke, Shreyash; Wong, Lydia Helena; England, Jason; Mhaisalkar, Subodh Gautam; Mathews, Nripan

2020

Ghosh, B., Febriansyah, B., Harikesh, P. C., Koh, T. M., Hadke, S., Wong, L. H., England, J., Mhaisalkar, S. G. & Mathews, N. (2020). Direct band gap mixed-valence organic-inorganic gold perovskite as visible light absorbers. Chemistry of Materials, 32(15), 6318-6325. https://dx.doi.org/10.1021/acs.chemmater.0c00345

https://hdl.handle.net/10356/146822

https://doi.org/10.1021/acs.chemmater.0c00345

This document is the Accepted Manuscript version of a Published Work that appeared in final form in Chemistry of Materials, copyright © American Chemical Society after peer review and technical editing by the publisher. To access the final edited and published work see https://doi.org/10.1021/acs.chemmater.0c00345

Downloaded on 28 Aug 2022 08:21:22 SGT

CHEMISTRY OF MATERIALS

pubs.acs.org/cm Article

Direct Band Gap Mixed-Valence Organic−inorganic Gold Perovskite as Visible Light Absorbers

Biplab Ghosh, Benny Febriansyah, Padinhare Cholakkal Harikesh, Teck Ming Koh, Shreyash Hadke, Lydia H. Wong, Jason England, Subodh G. Mhaisalkar, and Nripan Mathews*

Cite This: https://dx.doi.org/10.1021/acs.chemmater.0c00345 Read Online

ACCESS | Metrics & More | Article Recommendations | Supporting Information

ABSTRACT: Lead-free halide perovskite semiconductors are necessary due to the atmospheric instability and lead toxicity associated with the 3D lead halide perovskites. However, a stable lead-free perovskite with an ideal band gap (1.2−1.4 eV) for photovoltaics is still missing. In this work, we synthesized organic−inorganic gold halide double perovskites ($(CH_3NH_3)_2Au_2X_6$, X = Br, I) through a solution-processed route that offers an ideal direct band gap for photovoltaic applications. Density functional theory calculations confirm the direct nature of the band gap with reasonable absorption coefficients in the visible range and excellent charge transport properties. In addition, the Au-halide perovskites show high chemical stability and photoresponse. These combined properties demonstrate that Au-based halide perovskites can be a promising group of compounds for optoelectronic applications.

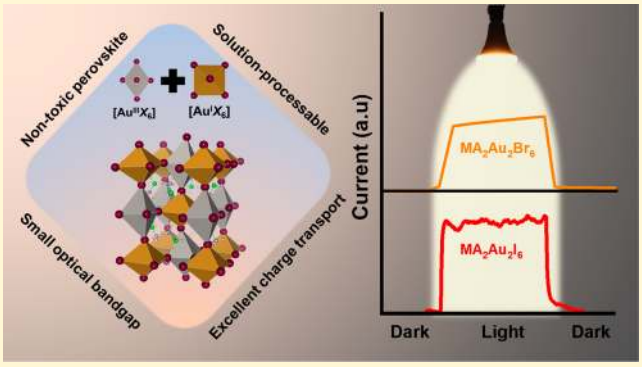

■ INTRODUCTION

Lead-based halide perovskites with the general formula of AMX_3 (A = protonated cation, M = Pb, X = Cl, Br, I) have emerged as one of the most promising semiconductor materials due to ease of fabrication, along with excellent optoelectronic properties. Although the atmospheric stability was poor at the beginning, subsequent research resulted in an unprecedented improvement in stability with a multication approach.[1,2] However, despite their rapid success in high-performance optoelectronic devices and reasonable stability, toxicity of the heavy metal (due to Pb^{2+}) remains a bottleneck in widespread commercialization. Given this issue, identifying a stable and nontoxic lead-free perovskite is now a key motivation and challenge for the perovskite community. Over the past decades, several lead-free perovskites and perovskite -derivatives have been proposed as potential substitutes for lead-based halide perovskites. Homovalent substitutions of lead with other metal ions carrying a +2 oxidation state such as Ge^{2+} or Sn^{2+} remain an excellent choice considering the ideal perovskite structure and the low band gap derived from these materials. However, both Ge- and Sn-based halide perovskites suffer from extreme instability.[3−5] Other metal cations with a +2 oxidation state are expected to exhibit inferior photovoltaic (PV) properties due to large optical band gaps.[5,6] Heterovalent substitutions with Bi^{3+} or Sb^{3+} offer much better atmospheric stability, but these halide compounds usually tend to crystallize into vacancy-ordered $A_3M_2X_9$ (M = Bi^{3+}, Sb^{3+}) structures, which exhibit poor PV performances due to low electronic dimensionality and large optical band gaps.[7−10]

To address these issues, cation-ordered double perovskites with the general formula of $A_2M'M''X_6$ (M′ and M″ are different metal cations with +1 and +3 oxidation states, respectively) have been proposed recently.[11] A notable example is $Cs_2AgBiBr_6$ which shows a long carrier lifetime and reasonable PV performances.[12−14] However, the optical band gaps of this family of compounds are large and indirect (1.9 to 2.2 eV).[15] Additionally, indirect band gap semiconductors require thicker absorber layers which are susceptible to nonradiative recombination, limiting their PV applications. Volonakis et al.[16] have synthesized a direct band gap $Cs_2InAgCl_6$ double perovskite, yet the compound does not absorb light in the visible region (measured band gap of 3.3 eV), thus making it unsuitable as a PV absorber. Among other double perovskites, In^+-based $Cs_2InBiCl_6$ and $Cs_2InSbCl_6$ have been predicted to have small direct band gaps and a small carrier effective mass. However, experimental validation of In^+-based double perovskites has not been realized yet.[17] Moreover, Xiao et al.[18] have demonstrated that In/Bi-based

Received: January 28, 2020
Revised: June 2, 2020
Published: June 3, 2020

ACS Publications © XXXX American Chemical Society

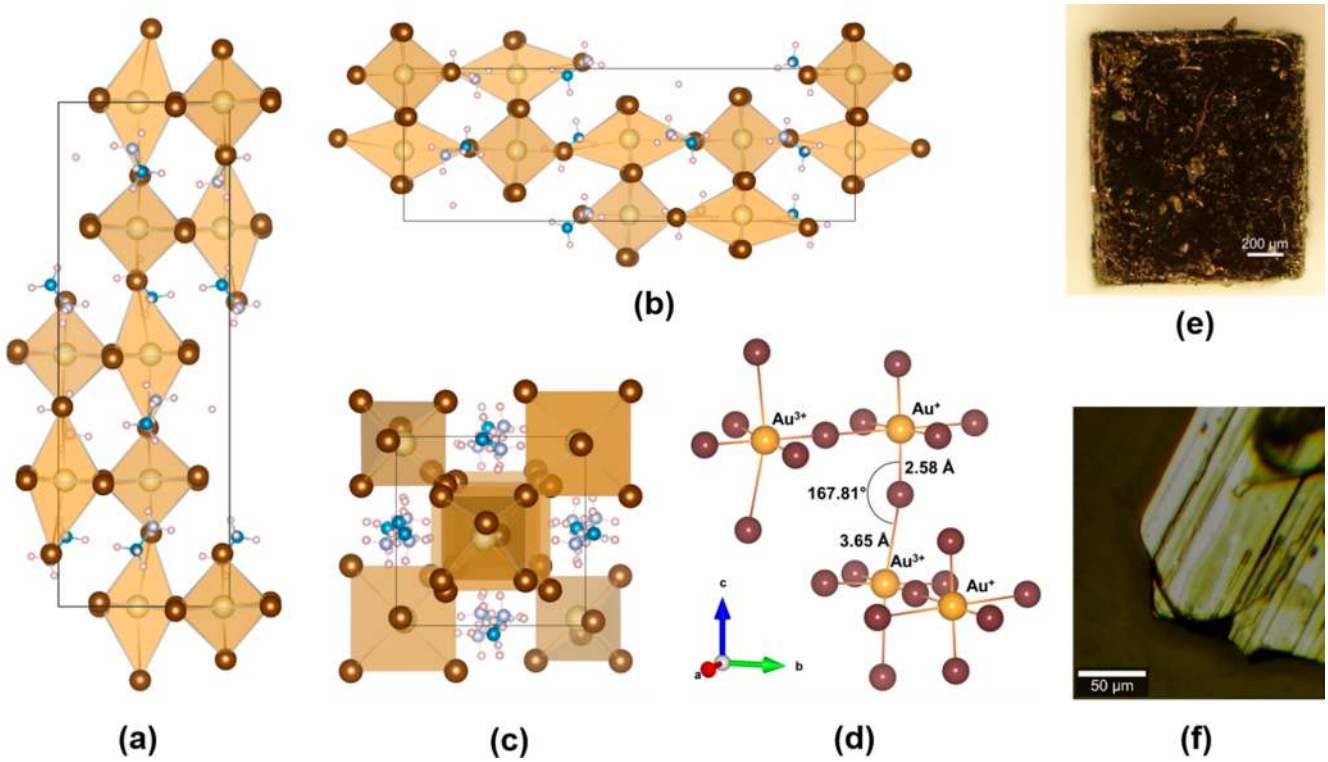

Figure 1. Polyhedral representations of the $MA_2Au_2I_6$ crystal structures. The crystal structure as viewed along the (a) *a*-axis, (b) *b*-axis, and (c) *c*-axis; (d) two relative orientations between linear $[Au^II_2]^-$ and square-planar $[Au^{III}I_4]^-$; and optical photograph of (e) $MA_2Au_2I_6$ and (f) $MA_2Au_2Br_6$ single crystals.

double perovskites suffer from inherent In vacancies, thus limiting their optoelectronic applications. Another interesting group of double perovskites is the mixed-valence perovskites in which a single metal cation with two different oxidation states (+1 and +3 for perovskite structure) is stacked alternatively to form a halogen-bridged perovskite structure. A notable example is $Cs_2Au_2X_6$ (X = Cl, Br, I) which was investigated in the early 2000s for its pressure-induced phase transition.[19] Debbichi et al.[20] have also predicted their excellent optoelectronic properties from density functional theory-based calculations. Interestingly, Au-based ternary halides also exhibit rich structural diversity. Recently, Worley et al.[21] reported several monovalent Au^{III}-based ternary halides with tunable optical band gaps. The hydrated compounds ($CH_3NH_3AuX_4{\cdot}H_2O$ (X = Cl, Br)) show layered structures with an optical band gap of 1.41 (X = Br) and 2.12 eV (X = Cl), whereas nonhydrated $CH_3NH_3AuCl_4$ shows a corner-shared crystal structure with a band gap of 2.14 eV. The apparently large band gap of monovalent compounds as compared to mixed-valence perovskites could be due to low electronic dimensionality, similar to Bi^{III}/Sb^{III}-based halide perovskites.[9] Here we report the synthesis of organic–inorganic hybrid mixed-valence Au-based double perovskites ($(CH_3NH_3)_2Au_2X_6$, X = Br, I) from a solution processing route. Contrary to low-dimensional Au^{III}-based hybrid perovskites, mixed-valence gold perovskites consist of three-dimensional metal-halide frameworks formed by elongated octahedra with Au^{III} and compressed octahedra with Au^I (Figure 1). These compounds, having direct and smaller band gaps, exhibit reasonable optical absorption in the visible region which offers new opportunities for lead-free perovskite materials in optoelectronic applications.

RESULTS AND DISCUSSION

To prepare single crystals of $(CH_3NH_3)_2Au_2I_6$, 2 mol of gold iodide (AuI) and 1 mol of methylammonium iodide (CH_3NH_3I) were mixed in 10 mL pf aqueous hydroiodic acid (48% in H_2O) solution and heated to 100 °C for dissolution. The resulting solution was filtered and kept in an oil bath at 100 °C. After slowly cooling to room temperature, black cuboid-shaped square crystals of $(CH_3NH_3)_2Au_2I_6$ are formed as shown in Figure 1e. For $(CH_3NH_3)_2Au_2Br_6$ single crystals, 1 mol of auric bromide ($AuBr_3$) and 2 mol of methylammonium bromide (CH_3NH_3Br) were dissolved in anhydrous ethanol at 100 °C. The solution was heated in an oil bath at 100 °C, and black single crystals were obtained by slow cooling of the solution (Figure 1f). It should be noted here that the crystals are hygroscopic and readily absorb moisture if exposed to ambient atmosphere.

Single-crystal X-ray diffraction (XRD) analysis reveals that $(CH_3NH_3)_2Au_2X_6$ (X = Br, I) crystallizes into the tetragonal perovskite structure (Figure 1a–c), with one of the unit cell axes being nearly triple the length of the other two (Table 1). The details of the crystal structure refinement data are

Table 1. Selected Crystallographic Parameters for $(CH_3NH_3)_2Au_2X_6$ (X = Br, I)

	$(CH_3NH_3)_2Au_2Br_6$	$(CH_3NH_3)_2Au_2I_6$
space group (number)	$P4_12_12$ (No. 92)	$P4_32_12$ (No. 96)
a (Å)	7.9115	8.3537
b (Å)	7.9115	8.3537
c (Å)	23.3850	24.6556
α, *β*, *γ*	90°	90°
volume (Å^3)	1463.71	1720.58

https://dx.doi.org/10.1021/acs.chemmater.0c00345
Chem. Mater. XXXX, XXX, XXX−XXX

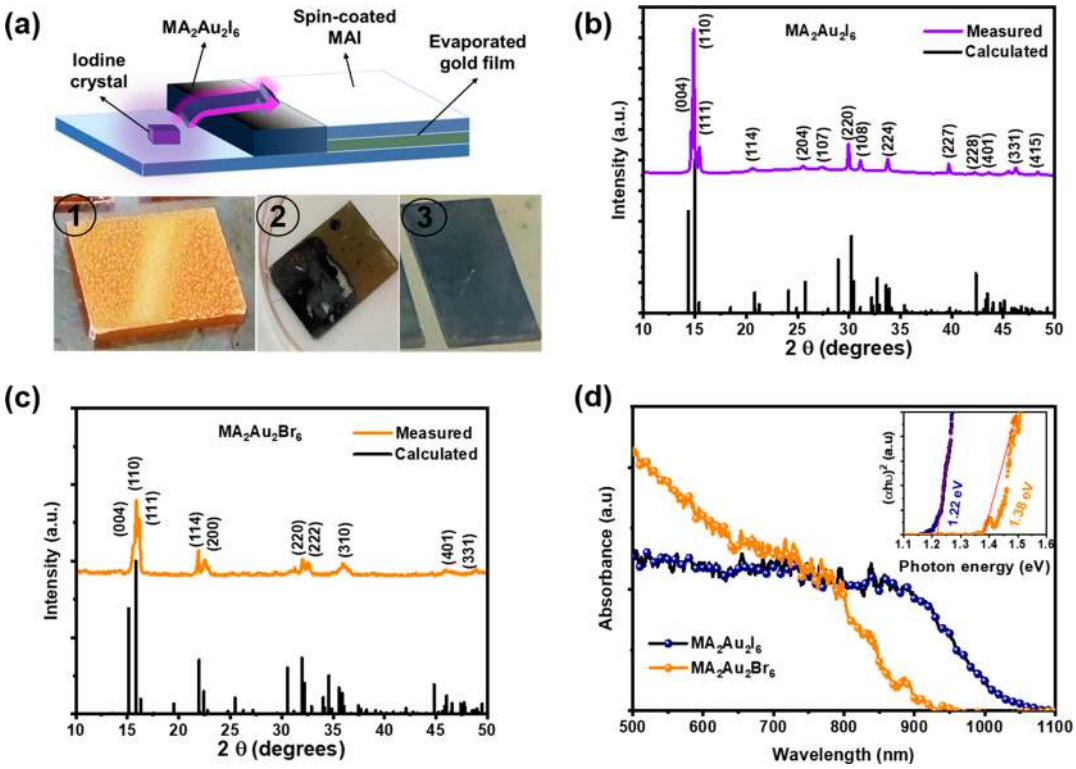

Figure 2. Physical and optical characterization of $MA_2Au_2X_6$ (X = Br, I) thin films. (a) Reactive polyiodide melt (RPM) method for synthesis of $MA_2Au_2I_6$ (bottom: 1, spin coated MAI on top of Au film; 2, partial conversion into $MA_2Au_2I_6$; and 3, complete conversion into $MA_2Au_2I_6$). Grazing-angle X-ray diffraction patterns of (b) $MA_2Au_2I_6$ and (c) $MA_2Au_2Br_6$ thin films. (d) UV−vis absorption spectra of Au-halide perovskites (inset: Tauc plot showing the direct nature of the band gaps).

provided in Table S1. Similar to conventional perovskite structures, $(CH_3NH_3)_2Au_2X_6$ (X = Br, I) are comprised of a three-dimensional framework of corner-connected haloaurate octahedra, with $CH_3NH_3^+$ molecules occupying the cuboctahedral cavities of the framework. Although the Goldschmidt's tolerance factor for gold halide perovskites is close to unity (see Text 1 in the Supporting Information), the octahedra are found to be heavily distorted. This is because, unlike $AM^{II}X_3$ perovskites, the gold perovskites are built of stacks of linear $[Au^IX_2]^-$ and square-planar $[Au^{III}X_4]^-$ complexes that alternate along all three [110], [1$\bar{1}$0], and [001] directions (Figure 1d). The presence of both Au^I and Au^{III} in the material was confirmed using X-ray photoelectron spectroscopy (XPS) (Figure S1).

The linear $[Au^IX_2]^-$ units in $(CH_3NH_3)_2Au_2X_6$ (X = Br, I) align perpendicularly to the plane of the $[Au^{III}X_4]^-$ centers, and they are connected to one another through long-range Au···X bonds. In the former case, this provides compressed octahedra, with equatorial Au···X distances (3.15 and 3.28 Å for Br^- and I^-, respectively) that are significantly longer than the axial Au−X bond lengths (2.41 and 2.58 Å for Br^- and I^-, respectively). Conversely, the $[Au^{III}X_4]^-$ centers form elongated octahedra with axial Au···X distances (3.51 and 3.65 Å for Br^- and I^-, respectively) that are much longer than the equatorial Au−X bond lengths (2.45 and 2.65 Å for Br^- and I^-, respectively). The bridging Au^I−I(Br)···Au^{III} angle (along the *c*-axis) of 167.81° (166.13°) is slightly bent. This distortion is analogous to that reported for the double perovskite $(CH_3NH_3)_2KBiCl_6$, in which it is attributed to the difference between the atomic radius of the K^I and and that of the Bi^{III} ions.[22] Given the large size difference between the Au^I and the Au^{III} ions resulting in tilting and rotation of the octahedron in addition to different bond lengths between Au^I−X and Au^{III}−X, a similar explanation for this distortion in the $(CH_3NH_3)_2Au_2X_6$ perovskites is likely the case. The distortions of the octahedra can be further quantified by the octahedral elongation (λ_{oct}) and angle variance (σ^2) as shown in Table S2.

To evaluate the applicability of these materials in thin-film optoelectronics, we attempted to fabricate thin films of hybrid Au-halide perovskites via a solution processing technique. As the auric (Au^{III}) iodide salt does not exist, we used AuI as the gold precursor. Dimethyl sulfoxide (DMSO) was used to dissolve the precursor salts, followed by spin coating and annealing at 100 °C to fabricate thin films. However, the resultant thin films exhibit poor surface coverage, along with Au metal as an impurity as shown in the XRD patterns (Figure S2). Interestingly, metallic gold is also found to precipitate during dissolution of AuI (Figure S2). Even after different solvent systems were employed, we were unable to deposit uniform thin films of $(CH_3NH_3)_2Au_2I_6$ by a conventional solution process. This is most probably hindered by the formation of metallic gold, which is most likely due to the use of a single Au^I precursor that disproportionates into Au^0 and Au^{III} (see Text 2 in the Supporting Information for details). We thus followed the reactive polyiodide melt (RPM) method[23,24] to convert metallic gold and MAI into Au-iodide perovskites as illustrated in Figure 2a. In brief, a nanoscale bilayer of MAI/Au is treated with iodine vapor that results in the formation of an MAI_3 melt which immediately converts the underlying Au into an $MA_2Au_2I_6$ perovskite. The photographs in Figure 2a show the gradual conversion of the MAI/Au

https://dx.doi.org/10.1021/acs.chemmater.0c00345
Chem. Mater. XXXX, XXX, XXX−XXX

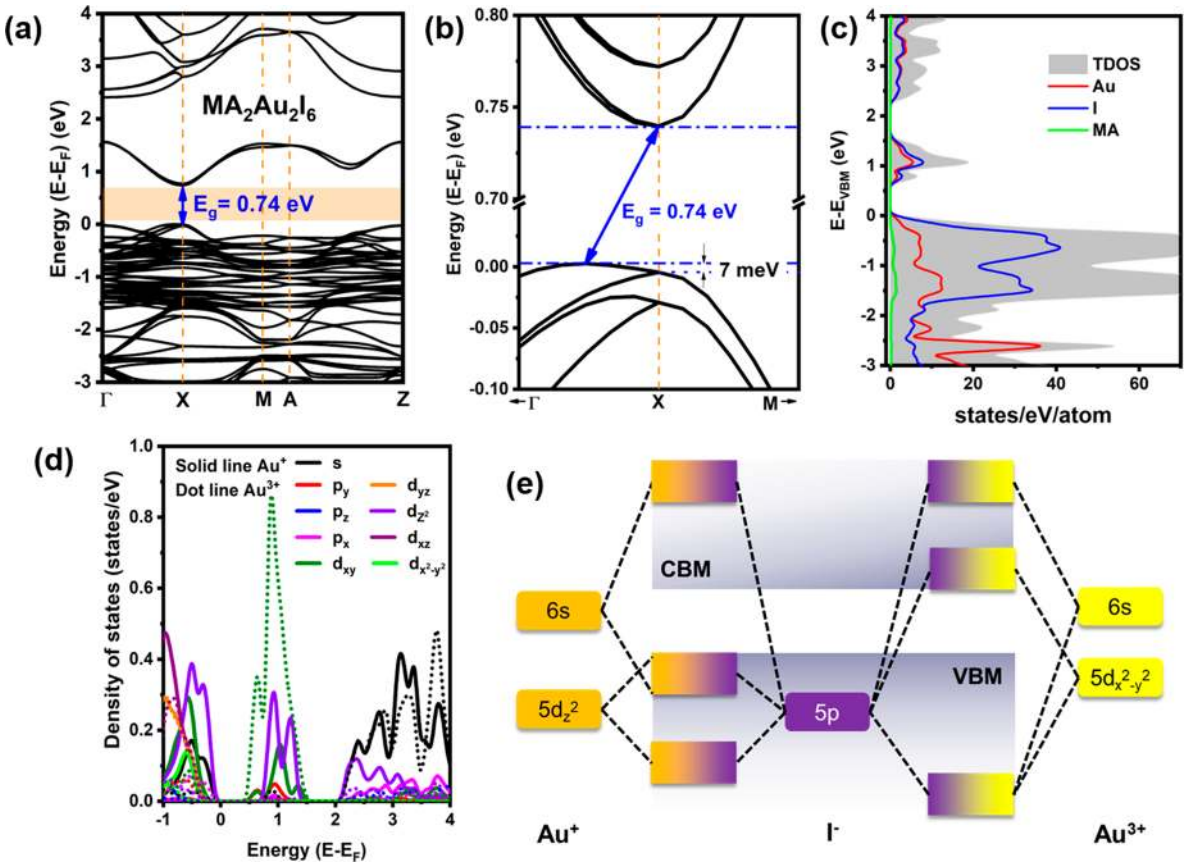

Figure 3. Calculated electronic structure of $MA_2Au_2I_6$ based on the PBE functional within DFT. (a) Electronic band structure of $MA_2Au_2I_6$ along high symmetry K-path, (b) magnified band gap region, showing a direct−indirect nature of the band gap near the X-point, (c) total and atomic partial density of states (PDOS) of each constituent element near the band edge, (d) PDOS of the d-orbital of two different Au centers (other orbitals are omitted for clarity), and (e) molecular orbital diagram showing hybridizations in $MA_2Au_2I_6$.

bilayer into the Au-iodide perovskite. Figure 2b illustrates the thin-film XRD patterns of $MA_2Au_2I_6$ fabricated via RPM, which shows no additional reflection from the Au metal. The top morphology of the thin film is shown in Figure S3a. On the other hand, thin films of $MA_2Au_2Br_6$ can be deposited by conventional solution processing via spin-coating of MABr and $AuBr_3$ dissolved in DMSO. Here, DMSO is most likely acting as a reducing agent to partially reduce Au^{III} to Au^{I} and promote the formation of $MA_2Au_2Br_6$ (possible mechanisms are highlighted in Text 2 in the Supporting Information). The thin films of $MA_2Au_2Br_6$, despite having nonuniform morphologies, exhibit pure phase formation without any Au metal impurity (Figure 2c and Figure S3b). The reference XRD patterns of hybrid gold perovskites were derived from the single-crystal XRD data. Both $MA_2Au_2Br_6$ and $MA_2Au_2I_6$ thin-film XRD patterns are in good agreement with the single-crystal data. Comparing the XRD patterns of the bromide and iodide perovskites, all the reflections observed are shifted toward lower 2θ values in bromides, which indicates an isostructural crystal structure with reduced lattice constants in $MA_2Au_2Br_6$. The band gaps of the $MA_2Au_2Br_6$ and $MA_2Au_2I_6$ thin films were estimated from ultraviolet−visible (UV−vis) absorbance spectroscopy measurements as shown in Figure 2d. Both compounds show sharp band edges, an indication of a direct band gap nature. Using a Tauc plot, the band gap energies of 1.22 and 1.38 eV are estimated for $MA_2Au_2I_6$ and $MA_2Au_2Br_6$, respectively (Figure 2d: inset). It should be noted here that the small hump in the inset figure is due to the instrumental artifact that arises due to a change in the detector. To further confirm the band gap, diffuse reflectance spectroscopy was carried out with the spectra shown in Figure S4a. Importantly, the band gap energies are much lower than those of conventional halide double perovskites, indicating that these materials are more practical for single junction PV. The low band gap of gold perovskites is attributed to the metal−ligand intervalence charge transfer (IVCT) between the $[Au^{I}X_2]^-$ and the $[Au^{III}X_4]^-$ groups.[25] The absorption coefficient, as calculated by the formula $\alpha = 2.303A/t$ (where A is the absorption and t is the thickness of the film), is estimated to be 1×10^3 cm^{-1} and 3×10^3 cm^{-1} for iodide and bromide, respectively, which is at least 1 order of magnitude smaller than that of $MAPbI_3$ (Figure S4b).

To confirm the nature of the band gap and the electronic properties of the hybrid gold perovskites, we calculated the electronic band structure using a generalized gradient approximation to density functional theory (GGA/DFT) using the P0BE functional.[26−31] Figure 3a illustrates the electronic band structure of $MA_2Au_2I_6$ along high symmetry points with an electronic band gap of 0.74 eV. The electronic band gap of $MA_2Au_2Br_6$ was calculated to be 1.04 eV (Figure S5a). The calculated band gaps are 0.47 and 0.4 eV smaller than experimental the values for the iodide and bromide perovskite, respectively, which is expected due to the use of the PBE functional. As pointed out by Debbichi et al.,[20] since there are no significant differences in the band dispersion based on PBE and computationally expensive Heyd−Scuseria−Ernzer-

https://dx.doi.org/10.1021/acs.chemmater.0c00345
Chem. Mater. XXXX, XXX, XXX−XXX

hof (HSE) results for $Cs_2Au_2I_6$, we expect similar trends for $MA_2Au_2X_6$ compounds. Additionally, we also observed similar effects with no change in the band dispersion with the inclusion of spin−orbit coupling (SOC), except the band gap of $MA_2Au_2I_6$ was further reduced (Figure S6). Hence, for this discussion, we only considered the electronic structure calculated using the PBE functional without SOC consideration. Although the band gap of $Cs_2Au_2I_6$ is predicted to be direct in nature in previous reports, our calculations reveal that the band gap of $MA_2Au_2I_6$ is direct−indirect in nature with a difference of 7 meV, which is much smaller than room-temperature thermal energy (Figure 3b). The conduction band minimum (CBM) is located at X, and the valence band maximum (VBM) is located along the X to Γ path (Figure 3b), resulting in a slightly indirect nature of the band gap. Hence, for practical purposes, $MA_2Au_2I_6$ should behave as a direct band gap material. Similar observations are found in $MAPbI_3$ where the direct−indirect nature of its band gap is found to be due to Rashba splitting.[32,33] Figure 3c illustrates the partial density of states (PDOS) plot for each constituent near the band edges. From the analysis of the PDOS, the MA^+ cation does not contribute near the band edges, a similar feature observed for conventional halide perovskite compounds. The valence band is predominantly comprised of I 5p states with a small contribution from Au 5d orbitals, while the conduction band is dominated by equal contribution from I and Au orbitals. Figure 3d further illustrates a detailed analysis of the PDOS of Au d orbitals. Based on our calculation, we propose a simple molecular orbital diagram of the hybridization in Au-based halide perovskites (Figure 3e). The top of the valence band essentially consists of antibonding orbitals from s and d_{z^2} orbitals from Au^I and I p orbitals. The antibonding nature of the VBM is often associated with defect-tolerant semiconductors, in which the acceptor-type defects form in resonance with the valence band.[34] The intermediate band forms the bottom of the conduction band, which results from the overlap of mainly $d_{x^2-y^2}$ orbitals of Au^{III} and p orbitals of I, with a small contribution from d_{z^2} orbitals of Au^I. As a result, a parity-forbidden band gap can be associated with the optical transition due to the contribution of Au^I d_{z^2} and Au^{III} $d_{x^2-y^2}$ in VBM and CBM, respectively. Although a parity-forbidden band gap is not suitable for a strong absorption coefficient, a strong joint density of states (JDOS), as shown in Figure 3c, results in a reasonable absorption coefficient in the visible range.[20] The top part of the conduction band is formed with equal contributions from the Au^I 6s and the Au^{III} 6s orbitals along with I p. In the bromide case, similar orbital contributions are observed with an increased electronic band gap (Figure S5b). Apart from the absorption coefficient, another key factor that can affect the performance in optoelectronic devices is the carrier mobility. We estimated the effective masses of Au-based halide perovskites by fitting the band dispersion curves to a parabolic function in the vicinity of the X point. The values are provided in Table S3. The relatively low effective mass of electrons (0.18 m_0, m_0 is the static electron mass) in the iodide perovskite indicates excellent charge transport properties, and the compound most likely possesses *n*-type behavior. On the other hand, the electron and hole effective mass in the bromide perovskite are nearly equal (0.27m_0 and 0.23m_0 for electron and holes, respectively), which indicates an ambipolar transport behavior. We have further validated the small effective mass using AC Hall measurement techniques. For iodide thin films, the estimated mobility of 0.85 ± 0.26 cm^2 V^{-1} s^{-1} (with N-type majority carriers and 8.95 × 10^{17} cm^{-3} carrier density) is comparable with the mobility of $MAPbI_3$. To shed light on the defect characteristics, a space-charge limited current (SCLC) technique was utilized. As shown in Figure S7, at low bias, the *I*−*V* trace shows an ohmic response, as confirmed by a linear fit. At higher bias, the injected free carrier concentration is still lower than the background carrier concentration, and the transport properties are controlled by trapping and detrapping of carriers, presented as the trap-SCLC region ($I \propto V^2$).[35] With increasing voltage beyond the trap filled limited voltage (V_{TFL}), the current increases sharply ($I \propto V^5$), indicating a trap-filling regime. However, as shown in Figure S6, even with a large applied voltage (123.5 V), the trap-free SCLC region was not obtained. The trap density of the as-grown Au-halide perovskite crystals was estimated by V_{TFL} to be η_{trap} = 3.35 × 10^{13} cm^{-3}, which is at least 2 orders of magnitude higher than conventional $MAPbI_3$ single crystals but comparable with established PV semiconductors such as cadmium telluride and copper indium gallium selenide.[36−38]

With promising optical and charge transport properties, we assessed the photoresponse of $MA_2Au_2X_6$ (X = Br, I) by characterizing the single crystals using a 2-point probe setup and measuring their current−voltage (*I*−*V*) characteristics under vacuum, as shown in Figure 4. The transient

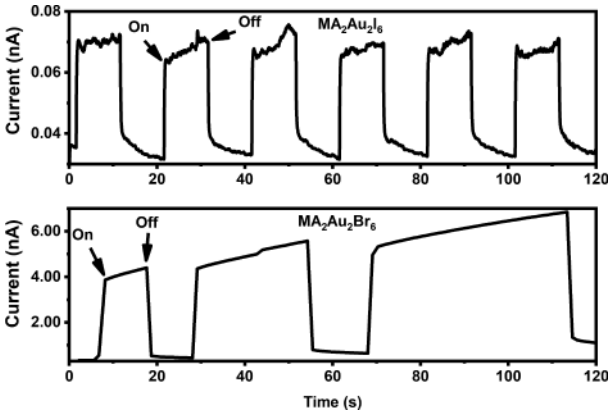

Figure 4. Transient photoconductivity curves of Au-halide perovskite single crystals under dark and simulated sunlight (100 mW cm^{-2}, AM 1.5). Photogenerated current under simulated white light over time at a fixed voltage of 1.0 V.

photoresponse was measured at a 1.0 V applied bias and indicated an increase in current under illumination. This is consistent with the notion that Au-based halide perovskites can be suitable for PV applications. In a step further, we also attempted the fabrication of perovskite solar cells with Au-based halide perovskites as the absorber layer in a device configuration of FTO/m-TiO_2/perovskite/PTAA/Au, where PTAA (poly(triaryl amine)) and m-TiO_2 (mesoporous titanium dioxide) were used as the hole- and electron-transport materials, respectively. However, the $MA_2Au_2I_6$ absorber layer was found to degrade quickly in ambient atmosphere due to the presence of moisture (Figure S8a,b). Being more stable than $MA_2Au_2I_6$, $MA_2Au_2Br_6$-based solar cell devices show a rectifying junction with an open-circuit voltage (V_{OC}) of 0.3 V (Figure S7c). The underlying reasons for poor performance of our proof-of-concept solar cell devices can be manifold. First of all, the absorption coefficient is at least one order smaller than

https://dx.doi.org/10.1021/acs.chemmater.0c00345
Chem. Mater. XXXX, XXX, XXX−XXX

that of $MAPbI_3$. This would necessarily require thicker films to absorb the full spectrum of Sun, similar to Si-based solar cells. However, extraction of the excited state carriers from thick films would also require a sufficiently large diffusion length and mobilities. Interestingly, the effective mass in Au-based halide perovskites is quite small, and the carrier mobilities are comparable to those of $MAPbI_3$. But the lack of photoluminescence from thin films and single crystals is an indication of the presence of traps within the material. The high background carrier concentrations are also not conducive to high efficiencies. It should be noted here that the films and single crystal degrade quickly in ambient atmosphere, which is another aspect in obtaining poor performance of our solar cells. At this stage, further studies are required to fully assess their potential and limitation of these material systems for photovoltaics. Through a rational examination of synthetic methodologies, precursor stoichiometry, additives, and appropriate device architectures, these low-band-gap Au-based halide perovskites will make their way into optoelectronic applications.

■ CONCLUSION

In conclusion, we have synthesized the novel mixed-valence double perovskites $MA_2Au_2X_6$ (X = Br, I) from a solution-processed route, enabled by the in situ disproportionation reaction of the Au ion. The Au-halide perovskites crystallize into a tetragonal crystal structure with connected octahedra in the 3D space. The perovskites display direct and tunable band gaps that can be ideal for optoelectronic applications, and the band gap is approximately 1.0 eV smaller than that of conventional halide double perovskites. The electronic structure calculation further shows reasonably good optoelectronic properties with low carrier effective mass. Although the Au-based halide perovskites are hygroscopic, the single crystals and thin films show no degradation in a controlled environment, thus signifying their high chemical stability. Additionally, the photoresponse of the single crystals, coupled with low trap density, indicates their potential in PV applications.

■ EXPERIMENTAL METHODS

Thin-Film Fabrication. AuI and $AuBr_3$ (99.9% pure and brought from Sigma-Aldrich) and MAI and MABr (99% pure and brought from GreatCell Solar) were used as received. For spin-coating $MA_2Au_2I_6$, stoichiometric amounts of MAI and AuI were dissolved in DMSO and spin-coated at 3000 rpm for 30 s. The films were later annealed at 100 °C for 10 min. For the reactive polyiodide method, around 30 nm Au was thermally evaporated on the desired substrates. The substrates were transferred into an Ar-filled glovebox, where 0.5 M MAI in IPA was spin-coated at 1000 rpm for 30 s. The substrates were treated with I_2 vapor to convert the MAI/Au bilayer into $MA_2Au_2I_6$ thin films. For $MA_2Au_2Br_6$ thin films, stoichiometric MABr and $AuBr_3$ were dissolved in DMSO and stirred overnight at 40 °C. The precursor solution was spin-coated onto desired substrates in an Ar-filled glovebox and annealed for 120 °C for 10 min.

Single Crystal Characterizations. A Bruker Quest CPAD area detector diffractometer (Bruker X8 CCD diffractometer) was used to analyze the single crystals using a IμS 3.0 Microfocus Mo Kα source (λ = 0.71073 Å), at 100 K. The crystal structures were resolved by direct methods and refined using the Bruker SHELXTL-2014 software package.

Thin-Film Characterizations. A Bruker D8 Advanced diffractometer (Bragg−Brentano geometry) with Cu Kα radiation (λ = 1.5418 Å) was used to characterize the thin-film crystal structure at room temperature. The thin-film morphologies were studied using a field emission scanning electron microscope (JEOL, JSM-7600F, operated at 5 kV). An ultraviolet−visible spectrophotometer (Shimadzu-3600) with an integrated sphere attachment (ISR-3100) and a 20 nm slit width was used for absorption spectroscopy in the wavelength range of 300−1200 nm. The XPS measurements were performed using a Kratos analytical instrument under UHV conditions with a 1486.6 eV monochromated Al K source. The elemental peaks were fitted with a Gaussian−Lorentzian profile with a Shirley background. AC Hall measurement was performed using a rotating parallel dipole line, followed by Fourier spectral analysis and lock-in detection of the Hall signal.[39,40]

***I*−*V* Measurement.** Current−voltage characteristics were measured using a Keithley 4200 SCS, with the single crystals sandwiched between two Au electrodes. The measurements were carried out in the dark and under a vacuum. The nonlinear response was analyzed according to SCLC theory. The trap density was calculated using the following equation:

$$V_{TFL} = \frac{en_t d^2}{2\epsilon\epsilon_0} \quad (1)$$

where ϵ_0 is the vacuum permittivity, d is the thickness of the crystal, and ϵ is the dielectric constant (113 for $MA_2Au_2I_6$). The dielectric constant was estimated using the standard capacitance measurement.

■ ASSOCIATED CONTENT

Supporting Information

The Supporting Information is available free of charge at https://pubs.acs.org/doi/10.1021/acs.chemmater.0c00345.

Additional explanation, XRD, and SEM characterizations of thin films and solar cell device data (PDF)

Crystallographic data of $MA_2Au_2I_6$ (CCDC 1989207) (CIF)

Crystallographic data of $MA_2Au_2Br_6$ (CCDC 1989208) (CIF)

■ AUTHOR INFORMATION

Corresponding Author

Nripan Mathews − *Energy Research Institute @ Nanyang Technological University (ERI@N), Singapore 637553; School of Materials Science and Engineering, Nanyang Technological University, Singapore 639798;* orcid.org/0000-0001-5234-0822; Email: nripan@ntu.edu.sg

Authors

Biplab Ghosh − *Energy Research Institute @ Nanyang Technological University (ERI@N), Singapore 637553;* orcid.org/0000-0002-5584-1830

Benny Febriansyah − *Energy Research Institute @ Nanyang Technological University (ERI@N), Singapore 637553*

Padinhare Cholakkal Harikesh − *Energy Research Institute @ Nanyang Technological University (ERI@N), Singapore 637553;* orcid.org/0000-0002-2488-1821

Teck Ming Koh − *Energy Research Institute @ Nanyang Technological University (ERI@N), Singapore 637553*

Shreyash Hadke − *Energy Research Institute @ Nanyang Technological University (ERI@N), Singapore 637553; Interdisciplinary Graduate School, Nanyang Technological University, Singapore 637371;* orcid.org/0000-0003-0964-4841

Lydia H. Wong − *Energy Research Institute @ Nanyang Technological University (ERI@N), Singapore 637553; School of Materials Science and Engineering, Nanyang Technological University, Singapore 639798;* orcid.org/0000-0001-9059-1745

Jason England − *Division of Chemistry and Biological Chemistry, School of Physical and Mathematical Sciences, Nanyang Technological University, Singapore 637371;* orcid.org/0000-0002-1525-4105

Subodh G. Mhaisalkar − *Energy Research Institute @ Nanyang Technological University (ERI@N), Singapore 637553; School of Materials Science and Engineering, Nanyang Technological University, Singapore 639798;* orcid.org/0000-0002-9895-2426

Complete contact information is available at: https://pubs.acs.org/10.1021/acs.chemmater.0c00345

Notes

The authors declare no competing financial interest.

■ ACKNOWLEDGMENTS

This research was supported by the National Research Foundation, Prime Minister's Office, Singapore, under its Competitive Research Programme (CRP Award No. NRF-CRP14-2014-03) and Intra-CREATE Collaborative Grant (NRF2018-ITC001-001). We would also like to thank Dr. Li Yongxin for helping us solve the crystal structures of the materials presented herein.

■ REFERENCES

(1) Correa-Baena, J.-P.; Saliba, M.; Buonassisi, T.; Grätzel, M.; Abate, A.; Tress, W.; Hagfeldt, A. Promises and challenges of perovskite solar cells. *Science* **2017**, *358* (6364), 739−744.

(2) Turren-Cruz, S.-H.; Hagfeldt, A.; Saliba, M. Methylammonium-free, high-performance, and stable perovskite solar cells on a planar architecture. *Science* **2018**, *362* (6413), 449−453.

(3) Noel, N. K.; Stranks, S. D.; Abate, A.; Wehrenfennig, C.; Guarnera, S.; Haghighirad, A.-A.; Sadhanala, A.; Eperon, G. E.; Pathak, S. K.; Johnston, M. B.; Petrozza, A.; Herz, L. M.; Snaith, H. J. Lead-free organic−inorganic tin halide perovskites for photovoltaic applications. *Energy Environ. Sci.* **2014**, *7* (9), 3061−3068.

(4) Kumar, M. H.; Dharani, S.; Leong, W. L.; Boix, P. P.; Prabhakar, R. R.; Baikie, T.; Shi, C.; Ding, H.; Ramesh, R.; Asta, M.; Graetzel, M.; Mhaisalkar, S. G.; Mathews, N. Lead-Free Halide Perovskite Solar Cells with High Photocurrents Realized Through Vacancy Modulation. *Adv. Mater.* **2014**, *26* (41), 7122−7127.

(5) Krishnamoorthy, T.; Ding, H.; Yan, C.; Leong, W. L.; Baikie, T.; Zhang, Z.; Sherburne, M.; Li, S.; Asta, M.; Mathews, N.; Mhaisalkar, S. G. Lead-free germanium iodide perovskite materials for photovoltaic applications. *J. Mater. Chem. A* **2015**, *3* (47), 23829−23832.

(6) Meng, W.; Wang, X.; Xiao, Z.; Wang, J.; Mitzi, D. B.; Yan, Y. Parity-Forbidden Transitions and Their Impact on the Optical Absorption Properties of Lead-Free Metal Halide Perovskites and Double Perovskites. *J. Phys. Chem. Lett.* **2017**, *8* (13), 2999−3007.

(7) Harikesh, P. C.; Mulmudi, H. K.; Ghosh, B.; Goh, T. W.; Teng, Y. T.; Thirumal, K.; Lockrey, M.; Weber, K.; Koh, T. M.; Li, S.; Mhaisalkar, S.; Mathews, N. Rb as an Alternative Cation for Templating Inorganic Lead-Free Perovskites for Solution Processed Photovoltaics. *Chem. Mater.* **2016**, *28* (20), 7496−7504.

(8) Xiao, Z.; Meng, W.; Wang, J.; Mitzi, D. B.; Yan, Y. Searching for promising new perovskite-based photovoltaic absorbers: the importance of electronic dimensionality. *Mater. Horiz.* **2017**, *4* (2), 206−216.

(9) Ghosh, B.; Wu, B.; Mulmudi, H. K.; Guet, C.; Weber, K.; Sum, T. C.; Mhaisalkar, S.; Mathews, N. Limitations of $Cs_3Bi_2I_9$ as Lead-Free Photovoltaic Absorber Materials. *ACS Appl. Mater. Interfaces* **2018**, *10* (41), 35000−35007.

(10) Mitzi, D. B. Organic-Inorganic Perovskites Containing Trivalent Metal Halide Layers: The Templating Influence of the Organic Cation Layer. *Inorg. Chem.* **2000**, *39* (26), 6107−6113.

(11) Zhao, X.-G.; Yang, J.-H.; Fu, Y.; Yang, D.; Xu, Q.; Yu, L.; Wei, S.-H.; Zhang, L. Design of Lead-Free Inorganic Halide Perovskites for Solar Cells via Cation-Transmutation. *J. Am. Chem. Soc.* **2017**, *139* (7), 2630−2638.

(12) Gao, W.; Ran, C.; Xi, J.; Jiao, B.; Zhang, W.; Wu, M.; Hou, X.; Wu, Z. High-Quality $Cs_2AgBiBr_6$ Double Perovskite Film for Lead-Free Inverted Planar Heterojunction Solar Cells with 2.2% Efficiency. *ChemPhysChem* **2018**, *19* (14), 1696−1700.

(13) Wu, C.; Zhang, Q.; Liu, Y.; Luo, W.; Guo, X.; Huang, Z.; Ting, H.; Sun, W.; Zhong, X.; Wei, S.; Wang, S.; Chen, Z.; Xiao, L. The Dawn of Lead-Free Perovskite Solar Cell: Highly Stable Double Perovskite $Cs_2AgBiBr_6$ Film. *Adv. Sci.* **2018**, *5* (3), 1700759.

(14) Slavney, A. H.; Hu, T.; Lindenberg, A. M.; Karunadasa, H. I. A Bismuth-Halide Double Perovskite with Long Carrier Recombination Lifetime for Photovoltaic Applications. *J. Am. Chem. Soc.* **2016**, *138* (7), 2138−2141.

(15) Filip, M. R.; Volonakis, G.; Giustino, F. Hybrid Halide Perovskites: Fundamental Theory and Materials Design. In *Handbook of Materials Modeling: Applications: Current and Emerging Materials*; Andreoni, W., Yip, S., Eds.; Springer International Publishing: Cham, 2018; pp 1−30.

(16) Volonakis, G.; Haghighirad, A. A.; Milot, R. L.; Sio, W. H.; Filip, M. R.; Wenger, B.; Johnston, M. B.; Herz, L. M.; Snaith, H. J.; Giustino, F. $Cs_2InAgCl_6$: A New Lead-Free Halide Double Perovskite with Direct Band Gap. *J. Phys. Chem. Lett.* **2017**, *8* (4), 772−778.

(17) Xiao, Z.; Du, K.-Z.; Meng, W.; Wang, J.; Mitzi, D. B.; Yan, Y. Intrinsic Instability of $Cs_2In(I)M(III)X_6$ (M = Bi, Sb; X = Halogen) Double Perovskites: A Combined Density Functional Theory and Experimental Study. *J. Am. Chem. Soc.* **2017**, *139* (17), 6054−6057.

(18) Xiao, Z.; Yan, Y.; Hosono, H.; Kamiya, T. Roles of Pseudo-Closed s2 Orbitals for Different Intrinsic Hole Generation between Tl−Bi and In−Bi Bromide Double Perovskites. *J. Phys. Chem. Lett.* **2018**, *9* (1), 258−262.

(19) Norimichi, K. Gold Valence Transition and Phase Diagram in the Mixed-Valence Complexes, $M_2[AuIX_2][AuIIIX_4]$ (M = Rb, Cs; X = Cl, Br, and I). *Bull. Chem. Soc. Jpn.* **2000**, *73* (7), 1445−1460.

(20) Debbichi, L.; Lee, S.; Cho, H.; Rappe, A. M.; Hong, K.-H.; Jang, M. S.; Kim, H. Mixed Valence Perovskite $Cs_2Au_2I_6$: A Potential Material for Thin-Film Pb-Free Photovoltaic Cells with Ultrahigh Efficiency. *Adv. Mater.* **2018**, *30* (12), 1707001.

(21) Worley, C.; Yangui, A.; Roccanova, R.; Du, M.-H.; Saparov, B. $(CH_3NH_3)AuX_4{\cdot}H_2O$ (X = Cl, Br) and $(CH_3NH_3)AuCl_4$: Low-Band Gap Lead-Free Layered Gold Halide Perovskite Materials. *Chem. - Eur. J.* **2019**, *25* (42), 9875−9884.

(22) Wei, F.; Deng, Z.; Sun, S.; Xie, F.; Kieslich, G.; Evans, D. M.; Carpenter, M. A.; Bristowe, P. D.; Cheetham, A. K. The synthesis, structure and electronic properties of a lead-free hybrid inorganic−organic double perovskite $(MA)_2KBiCl_6$ (MA = methylammonium). *Mater. Horiz.* **2016**, *3* (4), 328−332.

(23) Petrov, A. A.; Belich, N. A.; Grishko, A. Y.; Stepanov, N. M.; Dorofeev, S. G.; Maksimov, E. G.; Shevelkov, A. V.; Zakeeruddin, S. M.; Graetzel, M.; Tarasov, A. B.; Goodilin, E. A. A new formation strategy of hybrid perovskites via room temperature reactive polyiodide melts. *Mater. Horiz.* **2017**, *4* (4), 625−632.

(24) Turkevych, I.; Kazaoui, S.; Belich, N. A.; Grishko, A. Y.; Fateev, S. A.; Petrov, A. A.; Urano, T.; Aramaki, S.; Kosar, S.; Kondo, M.; Goodilin, E. A.; Graetzel, M.; Tarasov, A. B. Strategic advantages of reactive polyiodide melts for scalable perovskite photovoltaics. *Nat. Nanotechnol.* **2019**, *14* (1), 57−63.

(25) Kojima, N.; Hasegawa, M.; Kitagawa, H.; Kikegawa, T.; Shimomura, O. P-T Phase Diagram and Gold Valence State of the Perovskite-Type Mixed-Valence Compounds $Cs_2Au_2X_6$ (X = Cl, Br, and I) under High Pressures. *J. Am. Chem. Soc.* **1994**, *116* (25), 11368−11374.

(26) Kresse, G.; Furthmüller, J. Efficiency of ab-initio total energy calculations for metals and semiconductors using a plane-wave basis set. *Comput. Mater. Sci.* **1996**, *6* (1), 15−50.

(27) Kresse, G.; Hafner, J. Ab initio molecular dynamics for liquid metals. *Phys. Rev. B: Condens. Matter Mater. Phys.* **1993**, *47* (1), 558−561.
(28) Kresse, G.; Hafner, J. Ab initio molecular-dynamics simulation of the liquid-metal–amorphous-semiconductor transition in germanium. *Phys. Rev. B: Condens. Matter Mater. Phys.* **1994**, *49* (20), 14251−14269.
(29) Kresse, G.; Joubert, D. From ultrasoft pseudopotentials to the projector augmented-wave method. *Phys. Rev. B: Condens. Matter Mater. Phys.* **1999**, *59* (3), 1758−1775.
(30) Blöchl, P. E. Projector augmented-wave method. *Phys. Rev. B: Condens. Matter Mater. Phys.* **1994**, *50* (24), 17953−17979.
(31) Perdew, J. P.; Burke, K.; Ernzerhof, M. Generalized Gradient Approximation Made Simple. *Phys. Rev. Lett.* **1996**, *77* (18), 3865−3868.
(32) Wang, T.; Daiber, B.; Frost, J. M.; Mann, S. A.; Garnett, E. C.; Walsh, A.; Ehrler, B. Indirect to direct bandgap transition in methylammonium lead halide perovskite. *Energy Environ. Sci.* **2017**, *10* (2), 509−515.
(33) Hutter, E. M.; Gélvez-Rueda, M. C.; Osherov, A.; Bulović, V.; Grozema, F. C.; Stranks, S. D.; Savenije, T. J. Direct−indirect character of the bandgap in methylammonium lead iodide perovskite. *Nat. Mater.* **2017**, *16*, 115.
(34) Zakutayev, A.; Caskey, C. M.; Fioretti, A. N.; Ginley, D. S.; Vidal, J.; Stevanovic, V.; Tea, E.; Lany, S. Defect Tolerant Semiconductors for Solar Energy Conversion. *J. Phys. Chem. Lett.* **2014**, *5* (7), 1117−1125.
(35) Duijnstee, E. A.; Ball, J. M.; Le Corre, V. M.; Koster, L. J. A.; Snaith, H. J.; Lim, J. Toward Understanding Space-Charge Limited Current Measurements on Metal Halide Perovskites. *ACS Energy Lett.* **2020**, *5* (2), 376−384.
(36) Shi, D.; Adinolfi, V.; Comin, R.; Yuan, M.; Alarousu, E.; Buin, A.; Chen, Y.; Hoogland, S.; Rothenberger, A.; Katsiev, K.; Losovyj, Y.; Zhang, X.; Dowben, P. A.; Mohammed, O. F.; Sargent, E. H.; Bakr, O. M. Low trap-state density and long carrier diffusion in organolead trihalide perovskite single crystals. *Science* **2015**, *347* (6221), 519−522.
(37) Balcioglu, A.; Ahrenkiel, R. K.; Hasoon, F. Deep-level impurities in CdTe/CdS thin-film solar cells. *J. Appl. Phys.* **2000**, *88* (12), 7175−7178.
(38) Kerr, L. L.; Li, S. S.; Johnston, S. W.; Anderson, T. J.; Crisalle, O. D.; Kim, W. K.; Abushama, J.; Noufi, R. N. Investigation of defect properties in Cu(In, Ga)Se_2 solar cells by deep-level transient spectroscopy. *Solid-State Electron.* **2004**, *48* (9), 1579−1586.
(39) Gunawan, O.; Virgus, Y.; Tai, K. F. A parallel dipole line system. *Appl. Phys. Lett.* **2015**, *106* (6), 062407.
(40) Gokmen, T.; Gunawan, O. Hall measurement system with rotary magnet. US9041389B2, May 26, 2012.

https://dx.doi.org/10.1021/acs.chemmater.0c00345
Chem. Mater. XXXX, XXX, XXX−XXX